

Infrared period–luminosity relations of Galactic Miras based on multi-epoch photometry and the *Gaia* parallax uncertainty

S. Uttenthaler^{1,2,*}, T. Lebzelter², and S. Meingast²

¹ Institute of Applied Physics, TU Wien, Wiedner Hauptstraße 8-10, 1040 Vienna, Austria

² Department of Astrophysics, University of Vienna, Türkenschanzstraße 17, 1180 Vienna, Austria

Received February 16, 2026; accepted Month xx, 20yy

ABSTRACT

Context. Miras and other long-period variable (LPV) stars on the Asymptotic Giant Branch (AGB) follow period–luminosity (PL) relations. These relations have been difficult to study for Galactic LPVs because their distances were poorly known in the past.

Aims. We aim to establish the PL-relations of solar-neighbourhood Miras for several near-IR photometric bands.

Methods. To this end, we used multi-epoch photometry from the DIRBE and unTimely/WISE catalogues, *Gaia* parallax distances, and contemporary pulsation periods obtained from optical observations of a well-selected sample of solar-neighbourhood Miras.

Results. We show that clearly defined PL-relations in the nine investigated near-IR bands emerge from our data, for which we report slopes and zero-point magnitudes. We find that the Galactic Miras are fainter in the near-IR than their siblings in the Large Magellanic Cloud. We derive average period–temperature, period–bolometric-luminosity, and period–radius relations from fits to synthetic SEDs constructed from the PL-relations. By applying AGB evolutionary models, the scatter of stars around the PL sequences can also be used to test whether the parallax uncertainties quoted in the *Gaia* catalogue are realistic or underestimated. Furthermore, we performed such tests based on a comparison with parallaxes obtained with the VLBI and with a sample of LPVs in the globular cluster 47 Tuc.

Conclusions. We conclude that, for Galactic Miras with a fractional parallax uncertainty of ≤ 0.1 in the *Gaia* catalogue, the parallax uncertainty is underestimated by factors between 1.0 and 1.7, and most likely by ~ 1.3 . For more uncertain parallaxes, we find evidence that the distances (parallaxes) are generally overestimated (underestimated). Nevertheless, we find strong evidence that the large error inflation factors of AGB stars reported in the literature are unrealistic. Our results lend confidence to the parallax measurements of these highly extended, variable stars.

Key words. stars: AGB and post-AGB – stars: late-type – stars: evolution – stars: mass-loss – stars: oscillations

1. Introduction

Long-period variables (LPVs) are found on the upper part of the giant branch and are thus representing a late evolutionary stage of low- and intermediate-mass stars ($1 - 8M_{\odot}$). Their variability is caused by pulsational instabilities in their cool and extended outer envelopes. Pulsation proceeds in one or more radial or non-radial modes, and it is thus expected that LPVs follow a set of logarithmic period–luminosity (PL) relations in respective diagrams (Wood 2000). Long-time monitoring of stellar systems like the Magellanic Clouds opened the possibility to derive these relations observationally (e.g., Soszyński et al. 2004; Riebel et al. 2010; Soszyński & Wood 2013) because they host large populations of LPVs at nearly identical distances with relatively small and uniform interstellar extinction. Comparisons with pulsation models (e.g., Trabucchi et al. 2017) enable us to gain a deep understanding of fundamental aspects of AGB stars such as their stellar parameters, atmospheric structure, and mass loss.

Among the LPVs, the Mira variable class is of particular importance because these stars can be easily distinguished from other variables by their very large light amplitudes in the visual combined with long pulsation periods of 100 to 1000 days. Solar-neighbourhood Miras can thus be monitored even with amateur means (Karlsson 2013). There is a general consensus

today that Miras pulsate in the fundamental radial mode (Trabucchi et al. 2017) and form one of the prominent PL-relations.

In the past, the study of stellar systems such as the Magellanic Clouds (MCs) was most fruitful for the understanding of PL-relations of LPVs. As a result of the identical distances and similar reddening, the PL-relations are very well-defined and individual stars can be uniquely assigned to the respective relations (that is, pulsation mode) once their periods are known. Homogeneous, long-term surveys have provided periods and average magnitudes for LPVs in great numbers (e.g., Udalski 2003). In contrast, Galactic LPVs have received much less attention, because their distances were poorly known.

To measure the distances to LPVs in the solar neighbourhood, both ground- and space-based approaches were applied in the past decades. From the ground, Very Long Baseline Interferometry (VLBI) was used to measure the parallaxes, e.g., Nakagawa et al. (2016) and VERA Collaboration et al. (2020). Andriantsaralaza et al. (2022) established a bolometric PL-relation of Galactic Miras based on these VLBI parallaxes, but due to the extensive observational effort of this method and the limitation in the number of accessible objects, sample sizes are very small in these studies. Space based parallaxes for LPVs first became available with the Hipparcos mission. Again, the sample remained small and limited to the most nearby objects, and attempts to derive a PL-relation solely based on data for Galactic field stars remained non-conclusive (e.g., Glass & van Leeuwen 2007).

* Corresponding author: S. Uttenthaler,
stefan.uttenthaler@gmail.com

The study of Galactic LPVs was recently revived by the advent of large catalogues of parallax measurements provided by the *Gaia* space observatory (Gaia Collaboration et al. 2023). Lebzelter et al. (2023, see their Fig. 32) showed that the PL-relations of Galactic LPVs can be revealed when using the *Gaia* parallax measurements. Based on their *Gaia* catalogue and the 2MASS catalogue (Skrutskie et al. 2006), Sanders (2023) applied a probabilistic model to infer the Galactic Mira PL-relation in the 2MASS K band. This allows many insights and even the application of the Mira PL-relation to measure the local value of the Hubble constant (Huang et al. 2024). Such applications underline the importance of Mira PL studies much beyond the immediate field of the late phases of low-mass stellar evolution.

However, three important issues need to be mentioned that hamper observational derivation of a reference PL-relation for Miras to be used for comparison with models and for distance determination. First, Miras are strongly variable even in near-IR bands. Many studies largely rely on the single-epoch 2MASS photometry due to the challenge of observing a star's brightness variation over a year. However, the use of single-epoch measurements leads to a significant broadening of the observed PL-relations by variability scatter. Second, the LPV class is not homogeneous in mass like the Cepheids. The mass scatter leads to a widening of the PL-relation. Third, LPVs on the AGB are expected to have large parallax uncertainties due to their intrinsic properties. Surface brightness variations induced by large convective cells may significantly impact the measurement of the stellar photocentre and create noise in the *Gaia* astrometry (Chiavassa et al. 2018), since the radius of these stars is of the order of one astronomical unit. The stars are also intrinsically very red, and *Gaia*'s imaging system is not well-characterised for such red sources. Finally, Miras vary in colour during a pulsation cycle (Mowlavi et al. 2019), but the current DR3 astrometric pipeline uses a fixed colour. These measurement-related problems lead to an unclear effect on *Gaia* parallax uncertainty. Andriantsaralaza et al. (2022) suggest that the uncertainties are underestimated by as much as a factor of 5.44 for Miras brighter than $G = 8^m0$ on average. The crucial question of potentially underestimated *Gaia* parallaxes is lively discussed in the community (El-Badry et al. 2021).

In the present paper, we aim to provide PL-relations for nine near-IR bands, some of them for the first time, addressing the issue on photometric variability by adopting multi-epoch IR photometry of Galactic Miras available from two catalogues. We combine this photometry with period determinations from simultaneous optical observations of these Miras. By largely eliminating the variability-induced scatter of stars around the PL-relation, our approach allows us to address the third issue raised above, namely the question of underestimated parallax uncertainties, with special regard to Miras.

2. Data

2.1. Selection of the Mira sample

The first IR catalogue we use is the one published by Price et al. (2010). They extracted weekly averaged fluxes for 2652 stars from the cold and warm era all-sky maps of the Diffuse Infrared Background Experiment (DIRBE) onboard the Cosmic Microwave Background Explorer (COBE) satellite in four near-IR bands (1.25, 2.2, 3.5, and 4.9 μm). The cold and warm DIRBE eras span 3.6 years of observations, which is long enough to cover more than one cycle of even the longest-period fundamental-mode pulsators (Miras). We adopted their list of

variable and candidate variable stars from their Tables 1 and 2., comprising 597 objects in total. We call this the DIRBE catalogue in the following. According to Smith et al. (2004), DIRBE photometry of the brightest IR sources is ten times more precise than that of 2MASS, and the relations derived by the same authors suggest that the differences between the DIRBE and 2MASS filter systems are small enough to be neglected for our purposes.

The unTimely catalogue presented by Meisner et al. (2023) serves as the second source of IR photometry. It is a deep time-domain catalogue of detections based on Wide-field Infrared Survey Explorer (WISE; Wright et al. 2010) and NEOWISE observations in the $W1$ (3.4 μm) and $W2$ (4.6 μm) bands spanning ~ 10.5 years from 2010 through 2020. Most of the sample stars have been observed 16 times, with two observations in 2010 and two per year in the period 2014 to 2020, separated by about half a year. Assuming an approximately sinusoidal light curve, our numerical tests showed that the true mean brightness is much more precisely reconstructed, if it is calculated from the mean of the maximum and minimum flux, rather than from the mean of all ~ 16 observations of each star. The reason is that the sine wave is relatively flat around the extrema, but a quasi-random sampling at epochs away from the extrema, where the flux changes much more quickly with time, introduces significant uncertainty in the mean brightness. The average magnitudes of the stars were thus converted from the average of the maximum and minimum flux as given in the instructions in the unTimely catalogue based on the definition of nanomaggies (Finkbeiner et al. 2004).

Variability periods have been determined and listed by Price et al. (2010) for the DIRBE catalogue. However, for the unTimely sources, the cadence of observations is too low to determine reliable periods from the IR observations themselves, except for the longest-period stars. Therefore, we resorted to a compilation of Mira periods obtained from optical observations taken contemporaneously with the IR observations. We used the tables of the period evolution of 510 solar-neighbourhood Miras curated by T. Karlsson¹. The data collection is described in more detail in Karlsson (2013). The selection of stars is based on available observations in the AAVSO² database. Consequently, for historical reasons, more stars in the northern hemisphere than in the southern hemisphere are included. Additionally, stars must have 20 clear maxima documented to be included in the selection. Given this criterion, stars close to the ecliptic and objects with periods around one year may be under-represented in our sample: the former due to the longer annual observing gaps and the latter in cases where the maximum falls within these gaps. We thus inspected the location of the sample stars in the sky relative to the ecliptic, but found no indications for a selection effect. However, the period histogram of the sample stars shows a trough at periods slightly shorter than one year, suggesting that these objects are slightly under-represented in our sample.

Concerning selection effects, we have to stress that our sample is limited to optically bright Mira variables. This is a consequence of our need to minimize the effects of photometric variability in our Galactic PL-relations, which requires data sets only available for an optically bright sample of stars. Thus, stars with high mass-loss rates and strong circumstellar dust obscuration are naturally missing from this collection. This is favourable for our purpose, since we search for relations between period and brightness in individual photometric bands in the near-IR to be used as representatives of the P-L relation. This will only work

¹ <https://var.saaf.se/mirainfoper.php>

² <https://www.aavso.org/>

if the SED is not significantly affected by circumstellar dust. In summary, we consider the potential biases in the sample to be either relatively minor issues that are hard to avoid for any sample of solar-neighbourhood Miras with well-determined periods or to be favourable for our purposes.

We found that 132 stars in the DIRBE catalogue have periods listed in the Karlsson compilation. Conversely, we downloaded the WISE photometry for the 510 Karlsson Miras using the Python unTimely Catalog Explorer. We adopted the pulsation period with the Julian date closest to the mean date of the respective IR observations.

2.2. Preparation of the data

Both the DIRBE and the unTimely sample were cross-matched with the catalogue of *Gaia* distances and their 1σ uncertainties by Bailer-Jones et al. (2021), as well as the 2MASS catalogue (Skrutskie et al. 2006). Magnitudes in the DIRBE bands were calculated using the zero-magnitude fluxes given by Price et al. (2010). The photometry was de-reddened using the 3D map of Gontcharov (2017). As this map extends only out to 1200 pc from the sun, the extinction was set to this outer boundary for the more distant stars, which are few. We applied the extinction law of Xue et al. (2016) to the 2MASS and WISE bands. As no relative extinction values have been determined specifically for the DIRBE bands, we adopted the same relative extinction values for the [1.25] and [2.2] bands as for the 2MASS J and K bands, and we interpolated the extinction values to $A_{[3.5]}/A_{K_s} = 0.60$ and $A_{[4.9]}/A_{K_s} = 0.48$ from Fig. 18 of Xue et al. (2016) for the DIRBE [3.5] and [4.9] bands, respectively. The median extinction in the [2.2] band for the DIRBE gold sample (see below) is $0^m.09$; we are therefore confident that any other choice of extinction map or relative extinction values would have very modest effects on our results.

The uncertainties on the absolute magnitudes of the various DIRBE and WISE bands were determined by combining in quadrature the uncertainty induced by the distance measurement and the photometric uncertainty, where for the latter, we adopted the standard deviation of the mean of all observations of a star in a given band. Stellar spectral types were collected from the catalogue of Skiff (2014).

We defined a gold sample in all bands by setting a limit of 10% uncertainty on the *Gaia*-based distance measurement and by requiring a period available from the Karlsson compilation. We discarded one more star from the DIRBE sample, namely R For, which appears to be a faint outlier by more than 3σ in the DIRBE [2.2] band. This star was identified by Feast et al. (1984) as undergoing changes in circumstellar dust obscuration. An inspection of the AAVSO V band light curve shows that R For was in a relatively faint phase from 1990 to 1995, exactly when DIRBE observed it. Nevertheless, we did retain it for the derivation of the 2MASS K band PL-relation, as the 2MASS observations were taken some 10 years later, when the star was at its normal brightness again. This procedure retained a gold sample of 110 stars with DIRBE observations (91 M-, 9 MS/S-, and 10 C-type), and 312 stars with unTimely observations (253 M-, 28 MS/S-, 30 C-type, and one unknown spectral type). The DIRBE gold sample stars are at distances between 150 and 1550 pc, with a mean of 710 pc and a standard deviation of 340 pc, while the unTimely gold sample stars distribute between 150 and 3260 pc, with a mean of 1060 pc and a standard deviation of 560 pc. Thus, the unTimely gold sample is, on average, more distant than the DIRBE gold sample.

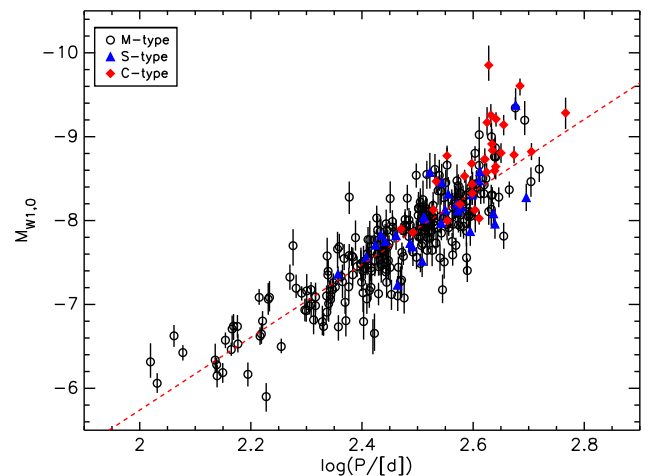


Fig. 1. PL diagram using the dereddened, absolute magnitude in the WISE $W1$ band, $M_{W1,0}$. Stars of different chemical spectral types are represented by different colours and symbol shapes; see the legend. The red dashed line is the linear least-square fit reported in Table 1.

We had to further restrict the gold sample in the $W2$ band because, despite the efforts in the unTimely catalogue to reconstruct the total flux of bright, partially saturated sources, it suffers from additional saturation effects. Plotting magnitude differences (colours) between the 2MASS K_s , $W1$, and $W2$ bands versus their magnitudes, we found that while $K_s - W1$ has no obvious dependence on apparent magnitude, colours involving the $W2$ band showed a significant linear trend for sources brighter than $W2 = 1^m4$. Thus, we excluded sources from the $W2$ gold sample brighter than this obvious saturation limit. This left us with 152 stars in the $W2$ gold sample (129 M-, 14 MS/S-, and 9 C-type stars).

This procedure ensured that the most obvious saturation effects were addressed. As has been shown by Schlafly et al. (2019, their Fig. 7), saturation sets in at $W1 = 8^m0$, and all our sample stars are brighter than this limit. In Sect. 3.3, we will make additional checks if the $W1$ and $W2$ fluxes are reliable in absolute terms. As we will also show below (e.g., Fig. 1), the WISE fluxes should be reliable at least in a relative sense among the stars.

3. Results

3.1. PL diagrams

Our main results are shown in Figs. 1 and 2. They show the dereddened, absolute magnitudes in the WISE $W1$ band ($M_{W1,0}$) and DIRBE [2.2] band ($M_{[2.2],0}$), respectively. Both samples exhibit well-defined sequences of increasing absolute magnitude with increasing pulsation period, as is known from many other works.

These are probably the best-defined PL-relations of substantial samples of Galactic Miras ever presented. The stars scatter around the least-squares linear fit (red dashed line, see Sect. 3.2) in the WISE $W1$ band with a standard deviation of $0^m.327$ and $0^m.313$ in the DIRBE [2.2] band, respectively. The same stars in Fig. 2 scatter with a significantly increased standard deviation of $0^m.378$ if the single-epoch 2MASS $K_{s,0}$ data are used, which corresponds to an additional scatter with standard deviation of $0^m.209$ added in quadrature. This additional scatter corresponds to the standard deviation of a sinusoidal curve with a full amplitude of $0^m.209 * 2 * \sqrt{2} = 0^m.592$, which should be a good measure

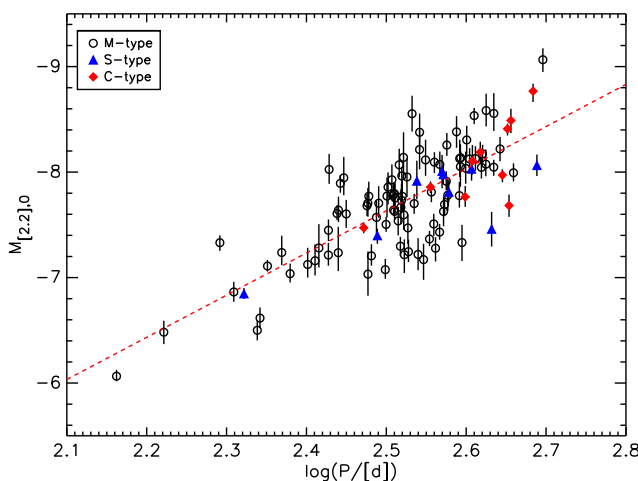


Fig. 2. Same as Fig. 1, but for the DIRBE [2.2] band, $M_{[2.2],0}$.

of the average amplitude of the stars in the K_S band. Applying sinusoidal fits to the DIRBE [2.2] band data, we find that the mean amplitude is $0^m.72$ and the median amplitude is $0^m.64$, which is in fair agreement with the predictions.

We experimented with the $W1$ photometry in a similar manner. To simulate the scatter of single-epoch $W1$ observations, we extracted only the last such observation from the tables and re-run the linear least-squares fit on these single-epoch observations. Here, the scatter increased from $0^m.327$ to $0^m.401$, corresponding to an additional scatter with a standard deviation of $0^m.234$ added in quadrature. This corresponds to the standard deviation of a sinusoidal curve with a full amplitude of $0^m.66$, which should again be representative of the average amplitude of the gold sample stars in the $W1$ band.

3.2. PL-relations

We determined for the gold samples the PL-relations in the DIRBE [1.25], [2.2], [3.5], and [4.9], the $3.4\mu\text{m}$ $W1$ and $4.6\mu\text{m}$ $W2$, as well as the 2MASS J , H , and K bands by ordinary linear least-squares fits, using the `SIXLIN.pro` GDL routine. As the uncertainties on the absolute magnitudes do not differ strongly and systematically, the data entered the fit with a uniform weight. We chose to compare the results with those of Whitelock et al. (2008), who also analysed a sample of Galactic Miras. Thus, we write the PL-relations in the form:

$$M_0 = b \times (\log P - 2.38) + a, \quad (1)$$

where b is the slope of the relation and a is the zero-point at $\log(P) = 2.38$. Other works applied quadratic rather than linear fits to the data (e.g., Yuan et al. 2017). We do not include a quadratic term because the PL diagrams do not suggest a deviation from a linear trend, most probably because our sample lacks very long-period Miras that are present in other works. Also, we do not make separate fits to the S and C stars because they are too few and they follow the trend of the M-type stars.

The results of our least-squares fits are collected in Table 1. The quoted uncertainties are the standard deviations as determined by the `SIXLIN.pro` routine. The relations are sorted by increasing effective wavelengths of the respective photometric band. From this sorting, we see that the slope of the relation b becomes steeper and the zero point a becomes brighter with increasing wavelength. This result is broadly consistent with those

Table 1. PL-relations of the form $M_0 = b \times (\log P - 2.38) + a$ (Eq. 1) of Galactic Miras in the NIR bands investigated here, sorted by increasing effective wavelength of the band.

Band	λ_{eff} (μm)	b	a
2MASS J	1.235	-2.653 ± 0.562	-5.926 ± 0.074
DIRBE [1.25]	1.25	-2.899 ± 0.445	-5.900 ± 0.065
2MASS H	1.662	-3.357 ± 0.449	-6.739 ± 0.062
2MASS K_S	2.159	-4.037 ± 0.351	-7.154 ± 0.052
DIRBE [2.2]	2.2	-3.997 ± 0.302	-7.153 ± 0.049
unTimely $W1$	3.368	-4.333 ± 0.154	-7.386 ± 0.022
DIRBE [3.5]	3.5	-4.798 ± 0.281	-7.493 ± 0.042
unTimely $W2$	4.618	-4.101 ± 0.190	-8.122 ± 0.025
DIRBE [4.9]	4.9	-4.924 ± 0.368	-7.739 ± 0.054

Table 2. PL-relations from the literature, converted to the form $M_0 = b \times (\log P - 2.38) + a$ (Eq. 1).

Ref.	Band	b	a	System
W08	K	-3.51 ± 0.20	-7.25 ± 0.07	Galaxy
R10	K_S	-3.31 ± 0.04	-7.485 ± 0.09	LMC
I21	$W1$	-3.807 ± 0.066	-7.554 ± 0.025	LMC
I21	$W2$	-3.794 ± 0.096	-7.751 ± 0.027	LMC

Notes. References: W08: Whitelock et al. (2008); R10: Riebel et al. (2010, their Sequence 1 for O-rich stars); I21: Iwanek et al. (2021b, their linear fit to the O-rich stars with $\log(P) \leq 2.6$).

reported by Riebel et al. (2010), Yuan et al. (2017), and Iwanek et al. (2021a, and references therein). In addition, the slopes and the zero points for the DIRBE [1.25] and the 2MASS J , as well as for the DIRBE [2.2] and the 2MASS K_S bands, agree very well within their uncertainties. In fact, the DIRBE [2.2] and the 2MASS K_S bands agree so well that we treat them as identical for the remainder of the paper.

We compare our results with those for the Galaxy and the Large Magellanic Cloud (LMC) reported in the literature and collected in Table 2. As our samples are dominated by O-rich Miras, we compared with literature results for O-rich Miras. The zero point of the PL-relation in the DIRBE [2.2] and K_S bands agrees very well with the one found by Whitelock et al. (2008) for O-rich Galactic Miras, to within $0^m.1$. We find a steeper slope than Whitelock et al. (2008), $b \simeq -4.0$ versus $b \simeq -3.5$, but their slope was fixed from a sample of LMC Miras. In fact, the slope reported by Riebel et al. (2010, their Sequence 1) for a sample of 2218 O-rich LMC Miras ($b = -3.31$) is in better agreement with the slope found by Whitelock et al. (2008). Assuming a distance modulus to the LMC of $\mu = 18^m.477$ (Pietrzyński et al. 2019), the zero point of the LMC Miras of Riebel et al. (2010) is brighter than that of the Galactic Miras by $\approx 0^m.235 - 0^m.332$. Sanders (2023) estimate that Galactic Miras are fainter than LMC Miras in the K_S band by $0^m.11$ at $P = 250\text{ d}$ ($\log P = 2.4$). We thus confirm the conclusion by Sanders (2023) that the near-IR PL-relations of O-rich Galactic Miras at short periods are steeper than those in the LMC and that Galactic Miras are fainter in these bands, suggesting that metallicity or population effects play a role.

Table 2 also contains the $W1$ and $W2$ relations of LMC Miras reported by Iwanek et al. (2021b). The zero point of the Galactic Miras in the $W1$ band is fainter than that of the LMC Miras by $0^m.168$. However, as we will show in Sect. 3.3 below, the $W1$ band may suffer from additional saturation effects, and we must take this result with a grain of salt. Taking the results for the $W2$

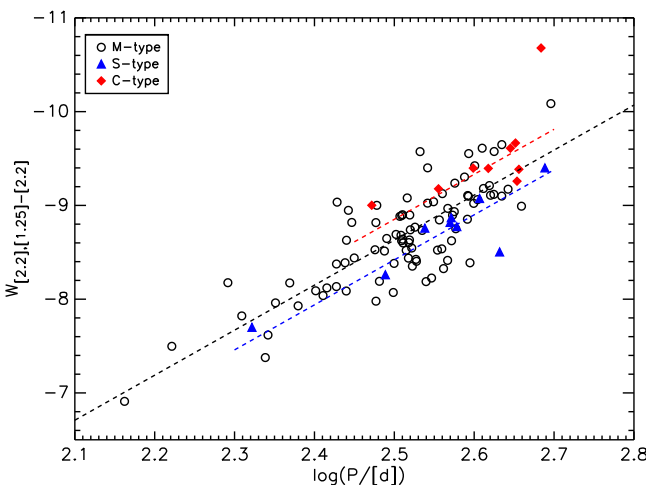


Fig. 3. DIRBE Wesenheit index $W_{[2.2],[1.25]-[2.2]}$ vs $\log P$ of the DIRBE gold sample. Stars of different chemical spectral types are represented by different colours and symbol shapes, see the legend. The dashed black, blue, and red lines show linear fits to the overall DIRBE gold sample, the S stars, and the C stars, respectively; see Table 3. The same slope as for the overall sample was adopted for the S and C stars.

band at face value, the Galactic Miras would be brighter than the LMC Miras of Iwanek et al. (2021b) by almost 0^m4 . However, the W_2 zero point does not comply well with the trend of monotonically increasing brightness with increasing wavelength visible in Table 1. As noted above, the W_2 band suffers from saturation, but we took this into account by eliminating stars with $W_2 < 1^m4$, keeping only 152 stars in the gold sample. The inspection of light curves of stars close to this saturation limit did not reveal any additional issues, and the $W_1 - W_2$ vs $M_{W1,0}$ colour-magnitude diagram looks inconspicuous. As we show in Sect. 3.3, the W_2 flux is significantly brighter than a Planck curve fit to the other data points. We conclude that the W_2 flux of our sample stars is significantly overestimated. We include the PL(W_2) relation in Table 2 only for completeness and urge the reader to use it with caution.

Finally, we constructed a Wesenheit index based on the DIRBE [1.25] and [2.2] photometry. It is defined as

$$W_{[2.2],[1.25]-[2.2]} = [2.2] - 0.686 \times ([1.25] - [2.2]). \quad (2)$$

The Wesenheit index eliminates the interstellar reddening component and a significant portion of the circumstellar reddening component, provided that the two extinction laws are not too dissimilar (Lebzelter et al. 2018). Figure 3 shows $W_{[2.2],[1.25]-[2.2]}$ of the DIRBE gold sample as a function of pulsation period. It is evident from this diagram that most of the C stars are brighter by $\sim 0^m2$ than the general trend defined by the M-type stars, whereas the S stars are all fainter than this trend, on average by $\sim 0^m2$. The number of C and S stars is too small to make a reliable linear least-squares fit to the data. Therefore, to fit their trend, we calculated their mean offset from the overall fit and adopted the slope derived from the M stars. For this, we excluded the C star S Cep, which is a very bright outlier. The coefficients of the Wesenheit index relations are presented in Table 3. While there is no clear luminosity difference between the S and C stars in, for example, the DIRBE [2.2] band, they differ by $\sim 0^m4$ in $W_{[2.2],[1.25]-[2.2]}$. The extinction correction makes the C stars appear much brighter than the S stars, likely due to the significantly higher circumstellar extinction of the former.

Table 3. Relations of the DIRBE Wesenheit index vs $\log P$, following the form $W_{[2.2],[1.25]-[2.2]} = b \times (\log P - 2.38) + a$.

Sample	b	a
DIRBE gold	-4.802 ± 0.339	-8.054 ± 0.052
S stars only	-4.802 ± 0.339^c	-7.843 ± 0.052
C stars only	-4.802 ± 0.339^c	-8.275 ± 0.052

Notes. ^c: Adopting the same slope as for the overall DIRBE gold sample.

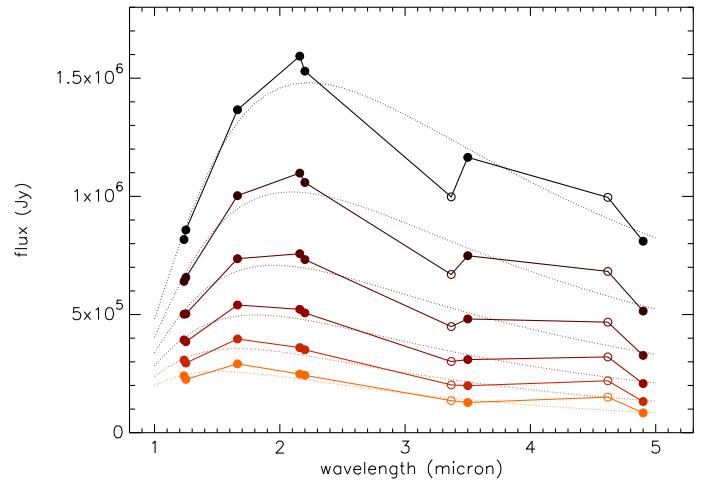


Fig. 4. Synthetic SEDs constructed with the PL-relations given in Table 1. The symbols connected by solid lines represent the fluxes derived for $\log(P) = 2.2, 2.3, 2.4, 2.5, 2.6$, and 2.7 (from bottom to top). The WISE bands are plotted as open symbols, while all other bands are plotted as filled symbols. The dotted lines are blackbody fits to each of the six synthetic SEDs, excluding the WISE bands.

3.3. Synthetic SEDs, period–temperature, period–bolometric-luminosity, and period–radius relation of Miras

With the help of the PL-relations in the nine IR bands we established above, we can construct mean synthetic spectral energy distributions (SEDs) at any $\log(P)$ value of our Mira sample. These synthetic SEDs will represent the average flux distribution of the sample Miras at this given period. We evaluated the PL-relations in Table 1 at $\log(P) = 2.2, 2.3, 2.4, 2.5, 2.6$, and 2.7 , which sample and represent the period distribution of our Mira stars well. The synthetic SEDs thus generated are shown in Fig. 4. The symbols connected by solid lines represent the synthetic SEDs at the six $\log(P)$ values.

The nine photometric bands span the wavelength range around the maximum emission of the sample stars. This allows us to make blackbody fits to the synthetic SEDs to derive additional (average) properties of Galactic Miras. The blackbody fits to the six synthetic SEDs are shown as dotted lines in Fig. 4. The WISE bands, which we plot as open symbols in Fig. 4, markedly deviate from the Planck curves: the W_1 band at $\sim 3.4 \mu\text{m}$ tends to fall below the blackbody fit, in particular at the long-period end, whereas the W_2 band at $\sim 4.6 \mu\text{m}$ tends to fall above the blackbody fit. Therefore, we decided to exclude both bands from the blackbody fits, even though including them would not significantly alter the results. As we are not aware of any (molecular) features in Mira spectra that could affect the flux in the two WISE bands so dramatically, we think that they deviate from the trend of the other bands because of remaining issues with reconstructing the flux of these bright, partially saturated objects.

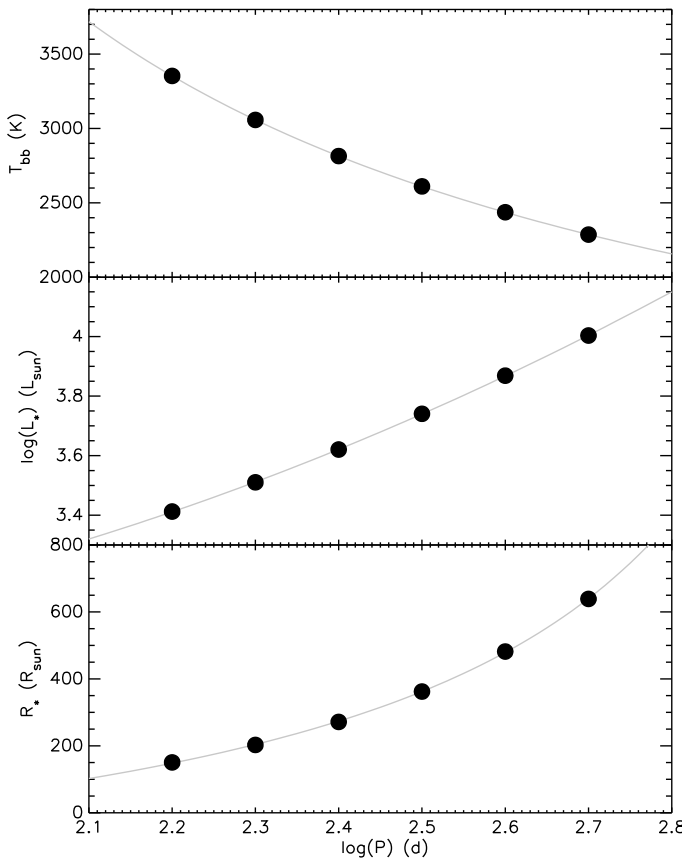


Fig. 5. Relations derived from the blackbody fits to the synthetic SEDs in Fig. 4. *Top panel:* blackbody temperature T_{bb} ; *middle panel:* logarithm of the stellar luminosity in solar units; *bottom panel:* stellar radius in solar units as a function of $\log(P)$. The grey lines show the relations given by Eq. 4, 5, and 6.

The blackbody temperature, T_{bb} , is a direct result of the fit of Planck curves to the synthetic SEDs. It varies between 3353 K at $\log(P) = 2.2$ and 2287 K at $\log(P) = 2.7$. We plot the best-fitting blackbody temperatures as a function of $\log(P)$ in the upper panel of Fig. 5. The run of T_{bb} as a function of $\log(P)$ may be fit by a function of the form

$$T_{\text{bb}} = \frac{c}{\log(P) + a} + b. \quad (3)$$

From a fit to T_{bb} at the six representative $\log(P)$ values, we find

$$T_{\text{bb}} = \frac{2895.3}{\log(P) - 1.2580} + 279.3. \quad (4)$$

This fitting function is plotted as a grey line in the top panel of Fig. 5. The individual points deviate by less than 0.5 K from this fit, with a root mean square (rms) of 0.3 K.

Furthermore, by integrating the Planck curve, we can calculate the bolometric luminosity of the synthetic SEDs and thus estimate the average luminosity of Miras at a given pulsation period to establish a period–bolometric-luminosity relation. Deriving the bolometric luminosity of the stars from a blackbody fit necessarily neglects absorption by atoms, molecules, and circumstellar dust grains, as well as dust emission in the mid-IR. However, as our sample exclusively contains optically bright Miras, at least the dust absorption and emission should be relatively modest. We regard the resulting luminosity as a fair estimate of the average bolometric luminosity of optical Miras at a given period. The period–bolometric-luminosity relation following from

our blackbody fits is shown in the middle panel of Fig. 5. The bolometric luminosity varies between $2584 L_{\odot}$ at $\log(P) = 2.2$ and $10079 L_{\odot}$ at $\log(P) = 2.7$. The relation is almost linear, but adding a quadratic term significantly improves the fit. We fit a parabola of the form

$$\log(L_{*}/L_{\odot}) = 3.506 - 1.044 \log(P) + 0.4551 \log(P)^2 \quad (5)$$

to the data points at the six representative $\log(P)$ values. The data deviates by at most $20 L_{\odot}$ from the fit, with an rms of $14 L_{\odot}$.

Finally, by applying the Stefan-Boltzmann law, $L = 4\pi R^2 T^4$, we can also calculate the average stellar radii. The results of this are shown in the lower panel of Fig. 5. For the six representative $\log(P)$ values, we find radii between $150 R_{\odot}$ at $\log(P) = 2.2$ and $639 R_{\odot}$ at $\log(P) = 2.7$. To fit the data, we choose a function of the same form as Eq. 3, which yields to the equation

$$R_{*}/R_{\odot} = \frac{-534.0}{\log(P) - 3.228} - 371.1. \quad (6)$$

The data deviate by at most $3 R_{\odot}$, with an rms of $2 R_{\odot}$. These relations may be useful for deriving average stellar properties in the study of individual objects or populations of Miras.

4. Testing the *Gaia* parallax uncertainties

In this section, we present three different approaches to test whether the parallax uncertainties of AGB stars provided by the *Gaia* DR3 catalogue are realistically estimated or if the uncertainties for this highly extended stellar type are underestimated. The first approach in Sect. 4.1 uses the rms scatter around the PL-relation in the DIRBE [2.2] band to test the uncertainties. The second approach in Sect. 4.2 takes a fresh look at the comparison with the parallaxes of AGB stars measured with VLBI methods. In doing so, we revisit the analysis by Andriantsaralaza et al. (2022). The last approach, presented in Sect. 4.3, uses the LPVs in the globular cluster 47 Tuc to test if their parallax uncertainties are potentially underestimated.

4.1. Estimating the parallax uncertainties from the PL(K) relation

The following test uses the astrophysical condition that Mira variables follow a (nearly) linear relation between the logarithm of the pulsation period and their absolute brightness. The magnitude of the scatter around the Mira PL sequences then depends on the uncertainty of the distance measurement used to derive the absolute brightness and any uncertainty in the variable's mean brightness. Since we minimized the uncertainty of the mean brightness by using light curve information, the scatter observed in our diagrams can be used to make an estimate of whether the parallax uncertainty is underestimated. For each star, we compute the quantity $f = \Delta M/\sigma_{m,\omega}$, where ΔM is the difference between each star's M_0 magnitude and the linear fit (Table 1) and $\sigma_{m,\omega}$ is the uncertainty in absolute magnitude originating from the parallax distance uncertainty. If the parallax uncertainty given in the *Gaia* catalogue is of the correct order, f should be close to 1. The standard deviation of this quantity thus allows to detect and quantify an underestimation of the parallax error. For the DIRBE gold sample in the [2.2] band, the standard deviation of f is 2.89. This is the maximum factor by which much the parallax distance uncertainty could be underestimated. Other bands have similar factors f ; in the DIRBE [3.5] band, it is 2.88, and in the $W1$ band, it is 2.74.

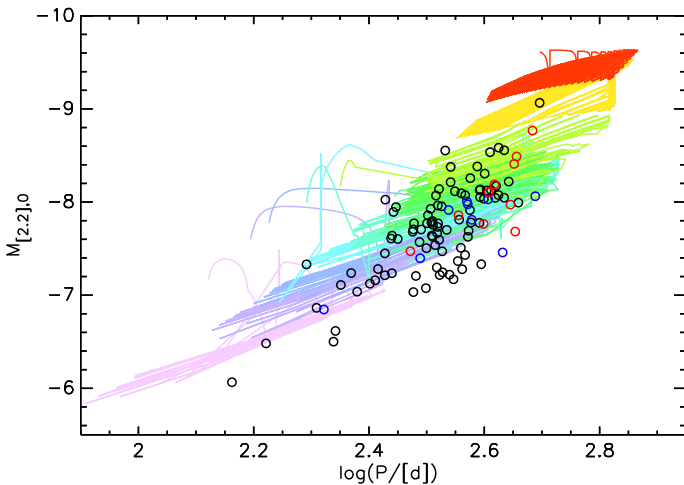


Fig. 6. Comparison of the COLIBRI model tracks with the DIRBE [2.2] gold sample in the PL(K) diagram. The tracks are plotted as lines with colours according to their initial masses between $1.0 M_{\odot}$ (pink line, lower left) and $5.0 M_{\odot}$ (red, upper right). The DIRBE [2.2] gold sample stars are plotted as open circles with their colours distinguishing chemical spectral types, cf. Fig. 2.

This simple estimate will only yield an upper limit to the error inflation factor (EIF) because it does not take into account the intrinsic width of the PL sequence. As AGB stars experience thermal pulse (TP) cycles, which are violent and quasi-periodic ignitions of their He-burning shells, evolutionary models predict that the stars will cross the pulsation sequence (here, we investigate only the fundamental mode sequence) on slanted paths. Depending on the initial mass, each of these TP cycles takes thousands or tens of thousands of years, and we do not know in which phase of its TP cycle an individual star is. Therefore, we have to model the intrinsic width of the fundamental mode sequence to constrain the EIF further.

For this estimate, we used a small grid of AGB evolutionary model tracks calculated with the COLIBRI code of Marigo et al. (2013) with a near-solar metallicity of $[Fe/H] = -0.03$ and masses of $M = 1.0, 1.3, 1.5, 1.8, 2.0, 2.4, 2.6, 3.0, 4.0$, and $5.0 M_{\odot}$. Based on these tracks, non-linear pulsation modes and periods were calculated with the analytic relations of Trabucchi et al. (2021). Only those parts of the tracks during which the model star pulsates in the fundamental mode were selected for the analysis. Each model time step i was assigned a weight $w_i \propto \Delta t_i \times M^{-2.3}$, where Δt_i is the time the model remains in that step, and the exponent $\alpha = -2.3$ corresponds to a 'Kroupa initial mass function' (Kroupa 2001). Furthermore, with this weighting, we assume a constant star-formation rate in the solar neighbourhood. All weights were normalised to a maximum of 1.0. The model tracks come with absolute magnitudes in several photometric bands, including the 2MASS bands (but not the WISE bands, for example). Thus, we can construct a theoretical PL(K) diagram with the non-linear pulsation periods and the $M_{K,S}$ magnitude, which we can treat as being identical to the DIRBE [2.2] band.

In Fig. 6, we compare the COLIBRI model tracks with the DIRBE [2.2] gold sample in the PL(K) plane. The model grid fills the plane without significant gaps. We see that the extension of the tracks at a given absolute magnitude reasonably resembles the observed width of the PL(K)-relation, and most stars in this diagram fall onto one of the model tracks.

In the next step, we constructed mean PL(K) relations from the model tracks. For this bootstrapping method, we selected

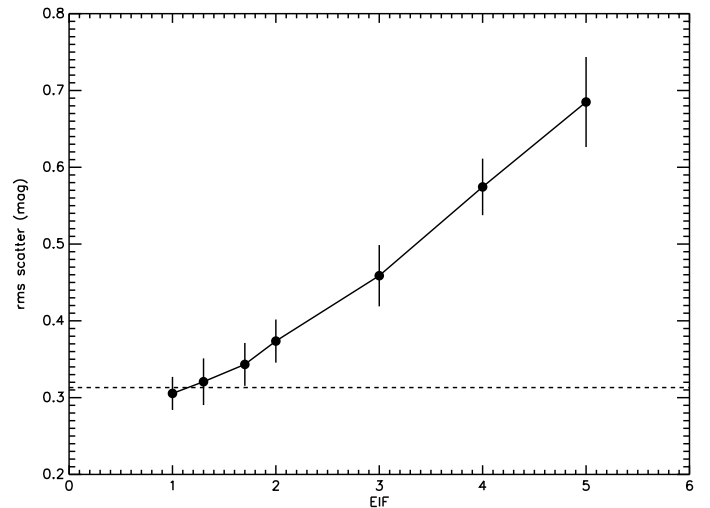


Fig. 7. RMS scatter around the simulated PL(K) relation of the COLIBRI evolutionary grid as a function of the EIF. The error bars indicate the 1σ range of the rms scatter of the 30 realisations for each EIF. The horizontal dashed line indicates the observed scatter of 0.313 around the PL-relation of the DIRBE [2.2] band shown in Fig. 2.

the same number of time steps (model stars) as we have observed stars in the DIRBE gold sample (110). A randomly selected model point i is kept in the model ensemble if its weight w_i is above the threshold formed by a uniformly drawn number x , $x \in [0, 1]$. To realistically model the PL(K) sequence, we added a normally distributed random scatter to $K_{S,i}$, for which we adopted a $\sigma_{K,S}$ with the same magnitude as a random one of the 110 observed parallax distance uncertainties of the DIRBE gold sample. This $\sigma_{K,S}$ was artificially inflated with EIFs between 1.0 and 5.0, where the latter was suggested by Andriantsaralaza et al. (2022). The photometric uncertainty, also derived from the observations of the gold sample, was added to this distance-based uncertainty in quadrature. However, the photometric uncertainty is clearly inferior to the parallax uncertainty. Thirty bootstrapping ensembles of 110 model steps were created for each chosen EIF, and the statistical scatter around a linear $\log P - M_{K,S}$ fit of each ensemble was evaluated. Note that this theoretical estimate does not take into account a distribution in the metallicity of the stars, the uncertainty in interstellar extinction, or other factors.

The result of our exercise is shown in Fig. 7, which plots the rms scatter around the simulated PL(K) relation of the COLIBRI evolutionary grid as a function of the EIF. It is not possible to precisely pinpoint how large the EIF of the AGB *Gaia* parallax uncertainties is. Nevertheless, we can see from Fig. 7 that the *Gaia* DR3 parallax uncertainties of the DIRBE gold sample (dashed line) are fully compatible with the scatter around the simulated PL(K) relation of the COLIBRI evolutionary grid, which means that the observed scatter is fully consistent with the uncertainties given in the *Gaia* catalogue. The uncertainties are also consistent with an EIF of 1.3 and marginally consistent with an EIF of 1.7. However, significantly larger EIFs can be safely excluded. At an EIF of 5, the PL-relation can hardly be recognised as a sequence of increasing brightness with an increasing pulsation period.

We caution, however, that our method to estimate the EIF from the scatter around the Mira PL(K) relation has shortcomings. The non-linear pulsation models of Trabucchi et al. (2021) have been tested on observations of LPVs in the Magellanic Clouds, but not for the higher metallicity of the Milky Way galaxy. Numerical tests by Trabucchi et al. (2021) have shown

that the non-linear pulsation periods derived from the analytic expressions predict those from the actual time series within a 10% error in more than 80% of the cases. This means that in some cases they deviate by more than 10% in the pulsation period. The dominant pulsation mode is selected based on the growth rates of the modes, and there may be considerable uncertainty in these. Furthermore, the models might not be so well-constrained at high masses ($M \gtrsim 4M_{\odot}$) as described in Trabucchi et al. (2021). From Fig. 6 we may, however, safely assume that the typical mass of solar-neighbourhood Miras is between 1 and $3 M_{\odot}$. Finally, the models of Trabucchi et al. (2021) approximate turbulent mixing in the envelope of AGB stars with the classical mixing length parameter. This mixing length parameter is neglected altogether in the analytic expressions used to calculate the non-linear periods of the model grid employed here. All these shortcomings may affect both the absolute values of brightnesses and periods and the range of variation in these two parameters along the PL-relation. Since our main interest is on the intrinsic scatter around this relation rather than its absolute location in the PL-plane, only the latter is relevant here. However, models do not allow to quantify the effect of these shortcomings on our conclusions yet.

Independently of the models, we can estimate from the magnitude of the rms scatter of stars around the PL-relation whether bright stars have more substantially underestimated parallax uncertainties than stars of lower brightness. We made this estimate with the unTimely $W1$ gold sample due to its larger size. We divided the gold sample at the median *Gaia* G band magnitude (8^m768) into two equal halves of 156 stars. The bright gold sample has an average relative distance uncertainty of 0.050, and the faint gold sample has 0.072. The rms scatter around the PL($W1$) relation of the two groups is 0^m311 and 0^m340 , respectively. Thus, the brighter stars have a smaller rms scatter, but they also have more precise parallaxes on average. The numbers do not suggest that the parallax uncertainties of the bright stars could be more severely underestimated than those of the faint stars.

4.2. Comparison of PL-relations based on *Gaia* and VLBI parallaxes

A direct comparison of parallax distances determined from *Gaia* and Very Long Baseline Interferometry (VLBI) of maser-emitting AGB stars can provide insight as to whether the combined uncertainty estimates are realistic. The parallax difference $\varpi_{\text{Gaia}} - \varpi_{\text{VLBI}}$, normalised by their quadratically combined uncertainties $\sqrt{\sigma_{\text{Gaia}}^2 + \sigma_{\text{VLBI}}^2}$, has been inspected for samples of AGB stars in the past to estimate parallax zero-point offsets and EIFs (Van Langevelde et al. 2018; Andriantsaralaza et al. 2022). Andriantsaralaza et al. (2022) provided arguments as to why the VLBI parallaxes and their associated uncertainties should be robust and highly accurate. They found an EIF of 4.20 for their entire AGB sample and an EIF of up to 5.44 for the optically brightest stars. However, from a purely theoretical point of view, we cannot know if the assumption of robustness of the VLBI parallax uncertainties is warranted. The EIF may actually have to be distributed to both the *Gaia* and the VLBI parallax uncertainties, or systematic uncertainties may affect the analysis.

We can gain additional insight into the robustness of *Gaia* and VLBI parallaxes and their uncertainties by inspecting PL diagrams of pulsating AGB stars constructed with the respective parallax distances. Such a diagram has been constructed by Andriantsaralaza et al. (2022, their Fig. 9) using VLBI parallaxes. However, we identified two problems with that diagram.

First, the bolometric magnitudes calculated by Andriantsaralaza et al. (2022) mainly rely on 2MASS single-epoch photometry. Most optical AGB stars have their emission maximum around the J , H , and K bands. Thus, these bands have a strong impact on the bolometric magnitudes, which will, therefore, exhibit increased scatter due to the non-negligible variability of the stars. To overcome this limitation, we used the mean unTimely $W1$ photometry to construct a PL($W1$) diagram; the typically 16 epochs of WISE observations significantly reduce the variability-induced scatter. Second, we found that the VSX pulsation periods (Watson et al. 2006) used by Andriantsaralaza et al. (2022) in some cases significantly disagree with the period in the databases we used. Therefore, we redetermined all periods of our sample stars based on light curves available from different sources. Where available, we adopted periods as listed by T. Karlsson. If that was not available, we determined the period from photometry available in the Kamogata/Kiso/Kyoto Wide-field Survey (KWS; Maehara 2014), the AAVSO, or The All Sky Automated Survey (ASAS; Pojmanski 2002) by a Fourier analysis of the light curves with the Period04 program (Lenz & Breger 2004). NSV 17351 has such a long pulsation period that the cadence of WISE observations is high enough to determine its period directly from the $W1$ light curve with the help of a simple sine fit. Finally, the period of the Mira OZ Gem is adopted from Heinze et al. (2018), who provide a light curve from which the reliability of the period was checked. We list the newly determined pulsation periods of the sample of AGB stars with VLBI parallaxes in Table 4 and compare them to the VSX period.

We added the three Miras R Cas, T UMa, and U CVn to the sample of Andriantsaralaza et al. (2022). Their VLBI parallaxes have been adopted from Vlemmings et al. (2003), Nakagawa et al. (2018), and the VERA Collaboration et al. (2020), respectively. Additionally, for NSV 17351, we adopted the VLBI parallax of $\varpi_{\text{VLBI}} = 0.247 \pm 0.035$ mas from Nakagawa et al. (2023).

The PL diagrams based on the VLBI and *Gaia* parallaxes are presented in Fig. 8, where the upper panel displays the results for the VLBI parallaxes and the lower panel those for the *Gaia* parallaxes. The comparison to the PL($W1$) relation determined from the gold sample displayed in Fig. 1 (dashed line in Fig. 8) confirms that the stars form a very well-defined Mira sequence, especially when using the VLBI parallaxes, but it is also well-behaved when adopting the *Gaia* parallaxes. By comparing the VSX periods with the newly determined periods in a PL diagram we concluded that the new periods also significantly reduce the scatter around a VLBI-based PL-relation. In this way, obvious outliers and overtone-mode pulsators can be clearly identified (see below). Many of the stars excluded by Andriantsaralaza et al. (2022) from determining the PL-relation do not need to be excluded when using the improved pulsation periods.

It is worth inspecting the few outliers in the relation. The four stars with $\log(P)$ near 2.2, namely BX Eri, RT Vir, RX Boo, and V637 Per, are semiregular variables (Table 4) and thus likely located on the first overtone PL relation. All other nominal non-Miras in the sample (HS UMa, HU Pup, RW Lep, S Crt, and SV Peg) appear to be fundamental-mode pulsators. QX Pup does not have a counterpart in the *Gaia* catalogue and, therefore, does not have a *Gaia* parallax. With its VLBI parallax, it is much below the PL sequence formed by the FM pulsators. QX Pup is also known as the Rotten Egg Nebula and is thought to be a protoplanetary nebula. Probably, it is so much dust-obscured that even the $W1$ band is significantly extinct. Because of the lack of a *Gaia* parallax, it is not included in the comparison of the PL relations and the estimation of the EIF (see below), and

Table 4. Improved pulsation periods of AGB stars with measured VLBI parallaxes, plotted in Fig. 8.

Object	Var.	P (VSX) (d)	P (new) (d)	Source
AP Lyn	M	730.0	433.9	KWS
BX Cam	M	486.0	439.4	AAVSO
BX Eri	SR	165.0	165.9	KWS
FV Boo	M	313.0	306.73	KWS
HS UMa	LB	0.0	331.1:	KWS
HU Pup	SRa	238.0	828.0	ASAS
NSV 17351	M	680.0	1108.0	unTimely
OZ Gem	M	598.0	603.72	H+2018
QX Pup	M	551.0	546.8	AAVSO
R Aqr	M	387.0	382.14	Karlsson
R Cas	M	430.6	431.00	Karlsson
R Cnc	M	357.0	364.86	Karlsson
R Hya	M	380.0	355.43	Karlsson
R Peg	M	378.1	377.93	Karlsson
R UMa	M	301.62	301.35	Karlsson
RR Aql	M	396.1	397.15	Karlsson
RT Vir	SRb	157.9	158.17	KWS
RW Lep	SRa	149.9	289.38	KWS
RX Boo	SRb	158.0	163.45	KWS
S CrB	M	360.26	359.79	Karlsson
S Crt	SRa	155.0	305.59	KWS
S Ser	M	371.84	367.08	Karlsson
SV Peg	SRb	144.6	318.34	KWS
SY Aql	M	355.92	357.36	Karlsson
SY Scl	M	411.0	415.83	KWS
T Lep	M	372.0	370.57	Karlsson
T UMa	M	256.35	256.79	Karlsson
U CVn	M	341.6	341.00	Karlsson
U Her	M	404.0	401.29	Karlsson
U Lyn	M	433.6	434.93	Karlsson
UX Cyg	M	569.0	577.86	Karlsson
V637 Per	SR	0.0	182.6:	KWS
V837 Her	M	514.0	525.93	KWS
W Leo	M	391.75	386.43	Karlsson
X Hya	M	299.5	298.20	Karlsson
Y Lib	M	277.0	275.14	Karlsson

Notes. Column 1: object name; column 2: variability type (M: Mira, SR/SRa/SRb: semi-regular variables, LB: irregular variables); column 3: pulsation period as reported in VSX (Watson et al. 2006); column 4: new period determination (this work); column 5: source for the data used for the new period determination: KSW: Kamogata/Kiso/Kyoto Wide-field Survey (Maehara 2014), AAVSO: <https://www.aavso.org/>, ASAS: The All Sky Automated Survey (Pojmanski 2002), unTimely: Meisner et al. (2023), H+2018: Heinze et al. (2018), Karlsson: Karlsson (2013).

also Andriantsaralaza et al. (2022) excluded it from determining their PL relation. UX Cyg is found somewhat above the PL-relation, both when using the *Gaia* and VLBI parallaxes. Also, HU Pup is significantly above the PL-relation, both when using the *Gaia* and VLBI parallaxes. It has a very long period of 828 d as we checked from the ASAS light curve, but it is not a Mira. Thus, possibly, it is a supergiant. Such massive stars are shifted to shorter periods and have amplitudes smaller than typical Miras (Lebzelter et al. 2019). It is thought that these stars also pulsate in the fundamental mode.

The longest-period star, NSV 17351, deserves special attention. The *Gaia* parallax ($\varpi_{\text{Gaia}} = 0.0884 \pm 0.1468$ mas) is actually

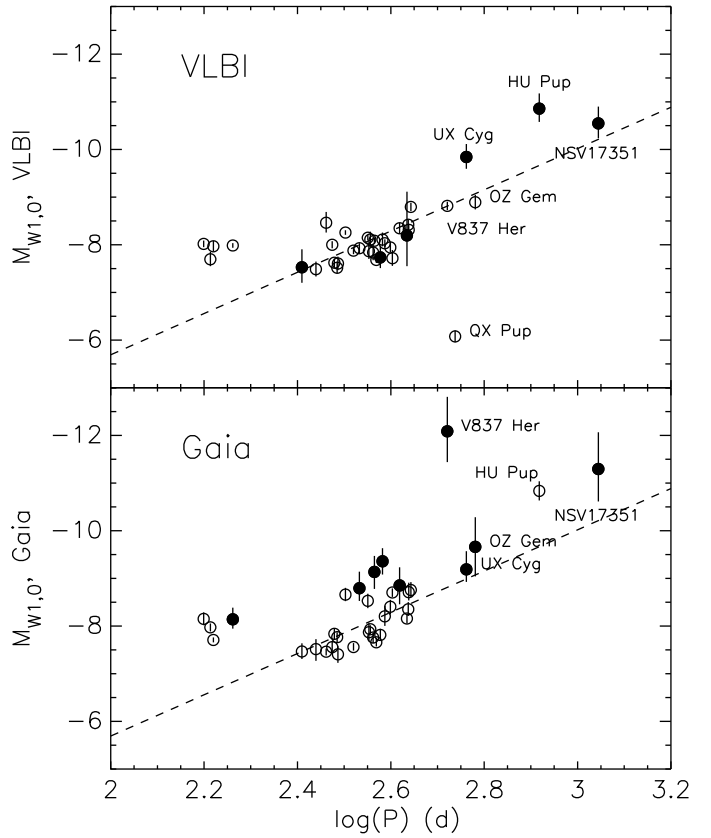


Fig. 8. PL(W1) of the sample stars from Andriantsaralaza et al. (2022). Top panel: $M_{W1,0}$ based on the VLBI parallax distance. Bottom panel: $M_{W1,0}$ based on the *Gaia* distance. Objects with $\log(P) \geq 2.65$ are identified by their names. Open symbols represent stars with $\sigma_{\varpi}/\varpi < 0.1$, filled symbols those with $\sigma_{\varpi}/\varpi \geq 0.1$, and the dashed line is the relation determined from the gold sample in Fig. 1 (cf. Table 1).

ill-defined, but the distance derived by Bailer-Jones et al. (2021) with the help of Bayesian statistics of ~ 5.7 kpc seems to be acceptable. When adopting the VLBI parallax of Nakagawa et al. (2023), NSV 17351 is consistent with being on the PL(W1) relation defined by the gold sample. NSV 17351 is an OH/IR star with a very long period of 1108 days determined from the unTimely W1 light curve. Nakagawa et al. (2023) report a period of 1122 ± 24 d based on H₂O maser flux measurements. There is a long-standing discussion in the literature about whether OH/IR stars at long periods ($P \gtrsim 1000$ d) follow the PL-relations of shorter-period Miras (e.g. Whitelock et al. 1991; Groenewegen 2022; Engels et al. 2024). The result for NSV 17351 argues in favour of the PL-relation extending to these long-period OH/IR stars.

A PL diagram of stars in the VLBI-sample (Fig. 8) can give us clues about the reliability of the *Gaia* and VLBI parallaxes and their uncertainties. It is particularly instructive to inspect the stars with the larger parallax uncertainties, $\sigma_{\varpi}/\varpi \geq 0.1$, represented by filled symbols in Fig. 8. In the PL(W1) diagram based on the VLBI parallaxes (upper panel), we see that those stars, even if they are few, do not systematically deviate from the PL-relation of the gold Mira sample indicated by the dashed line (we remind that HU Pup might be located above the PL(W1) relation intrinsically and four stars are likely first-overtone pulsators). Looking at the PL(W1) diagram based on the *Gaia* parallaxes, we find that almost all stars deviating from the PL sequence significantly show $\sigma_{\varpi}/\varpi \geq 0.1$, and all of them are shifted to higher luminosity, V837 Her even by a large margin. This indicates that

their distances are systematically overestimated (parallaxes are underestimated). Including these stars in a comparison with the VLBI parallaxes, as done by Andriantsaralaza et al. (2022), will necessarily increase the estimated EIF.

On the other hand, we find indications that some of the VLBI parallax uncertainties could be underestimated. As noted above, here we adopt the parallax measurement of NSV 17351 from Nakagawa et al. (2023). The uncertainty reported by these authors is 3.5 times larger than the one used by Andriantsaralaza et al. (2022). Six of the Andriantsaralaza et al. (2022) sample stars have VLBI parallaxes with reported uncertainties of 2% or better. In contrast, only two of the 312 unTimely W1 gold sample stars have relative *Gaia* parallax uncertainties slightly below 2%. It is advisable to check if the small VLBI uncertainties are indeed realistic (VERA Collaboration et al. 2020).

As previously done by Van Langevelde et al. (2018) and Andriantsaralaza et al. (2022), we can use this VLBI sample to test the reliability of the uncertainty estimates. Andriantsaralaza et al. (2022) assumed the VLBI parallax uncertainties to be robust and defined a one-sided error inflation factor (EIF) that applies to the *Gaia* parallax uncertainties only, such that the quantity

$$\frac{\Delta\varpi}{\sigma_{\varpi,\text{tot}}} = \frac{\varpi_{\text{Gaia}} - \varpi_{\text{VLBI}}}{\sqrt{(\text{EIF} \cdot \sigma_{\varpi}^{\text{Gaia}})^2 + (\sigma_{\varpi}^{\text{VLBI}})^2}} \quad (7)$$

has a distribution with a standard deviation of 1.0. Here, ϖ_{Gaia} and $\sigma_{\varpi}^{\text{Gaia}}$ are the *Gaia* parallax and its associated uncertainty, and ϖ_{VLBI} and $\sigma_{\varpi}^{\text{VLBI}}$ are the same for the VLBI measurements. As argued above, we do not a priori know that the VLBI parallaxes are estimated correctly and some of them could be underestimated. We therefore also define a symmetric or two-sided EIF ξ that applies to both *Gaia* and VLBI parallax uncertainties, such that the quantity

$$\frac{\Delta\varpi}{\sigma_{\varpi,\text{tot}}} = \frac{\varpi_{\text{Gaia}} - \varpi_{\text{VLBI}}}{\sqrt{(\xi \cdot \sigma_{\varpi}^{\text{Gaia}})^2 + (\xi \cdot \sigma_{\varpi}^{\text{VLBI}})^2}} \quad (8)$$

has a distribution with a standard deviation of 1.0. We do not apply a zero-point offset (ZPO) to correct the *Gaia* parallaxes ($\varpi_{\text{Gaia}}^{\text{corr}} = \varpi_{\text{Gaia}} - \text{ZPO}$) because we see that this is strongly driven by the two most nearby stars R Hya and RX Boo ($d \approx 150$ pc), which both have considerably larger VLBI parallaxes than *Gaia* parallaxes. This is most probably the reason why the ZPO determined by Andriantsaralaza et al. (2022, -0.131 mas) for their AGB star sample is significantly larger in absolute terms than those found by Lindegren et al. (2021, -0.021 mas) or Groenewegen (2021, -0.039 mas), which are negligible.

We calculated the one-sided and the symmetric EIF for different subsamples. Motivated by the results of the PL diagram (Fig. 8), we can choose to restrict the sample to stars with parallax-based distances with a relative uncertainty $\sigma_{\varpi}/\varpi \geq 0.1$ in both the *Gaia* and VLBI catalogues. This yields a sample of 22 stars. The one-sided EIF (Eq. 7) of that sample is 4.59, and the two-sided EIF (Eq. 8) is 2.40. However, this value is strongly driven by the numbers for U Her and RW Lep, which have parallaxes that significantly deviate between *Gaia* and VLBI observations. If we exclude them in the calculation of the EIFs, the factors decrease to 2.27 and 1.89, respectively.

In the next step, we consider the bright and faint stars separately. We split the sample in half at the median G band magnitude of 7^m922 . Besides U Her and RW Lep, we also exclude V837 Her from the faint sample because not only do the

Table 5. One-sided (EIF) and two-sided (ξ) error inflation factors to be applied to the *Gaia* parallax uncertainties to bring *Gaia* and VLBI parallaxes into statistical agreement, for different selections of stars.

Sample	N	EIF	ξ
$\sigma_{\varpi}/\varpi < 0.1$	22	4.59	2.40
$\sigma_{\varpi}/\varpi < 0.1 \setminus \{\text{U Her, RW Lep}\}$	20	2.27	1.89
$G \leq 7^m922 \setminus \{\text{U Her, RW Lep}\}$ ('bright')	16	2.69	2.17
$G > 7^m922 \setminus \{\text{V837 Her}\}$ ('faint')	16	1.76	1.64

Notes. Column 1: Definition of the subsample; column 2: number of stars in that subsample; column 3: one-sided EIF as defined by Eq. 7; column 4: two-sided EIF as defined by Eq. 8.

Gaia and VLBI parallaxes differ significantly (0.1771 mas and 1.09 mas, respectively) but also because its VLBI parallax uncertainty is extremely small (0.01 mas). As mentioned, QX Pup has no *Gaia* parallax. This yields 16 stars in both the bright and faint subsamples. Both the one-sided and the two-sided EIFs are considerably smaller in the faint sample. The results are collected in Table 5. We thus confirm the results by Andriantsaralaza et al. (2022) that the fainter stars require smaller EIFs be applied to their parallax uncertainties to bring the parallaxes into statistical agreement. In particular, the one-sided EIF of the faint sample is only 1.76, which is considerably smaller than the EIFs reported by Andriantsaralaza et al. (2022, their Table 2). However, we caution that the number of AGB stars that have parallaxes measured by *Gaia* and VLBI is still very small, generally limiting the conclusions that can be drawn from such comparisons.

4.3. *Gaia* parallaxes of 47 Tuc AGB variables

The reliability of *Gaia* parallax uncertainties can also be inspected with a sample of AGB stars that are members of a stellar system and are, thus, at an essentially identical distance. The Magellanic Clouds host a large population of AGB stars; unfortunately, they are too distant to reliably measure parallaxes. Galactic open clusters are too sparsely populated to host sufficient numbers of stars in the sort-lived AGB phase (see Marigo et al. 2022, for a recent collection of AGB stars in Galactic open clusters). Only nearby Galactic globular clusters are good candidates for assembling a large enough sample of AGB stars to test their *Gaia* parallaxes. The globular cluster 47 Tucanae (47 Tuc) hosts a significant population of LPVs on the AGB that has been extensively studied.

In using stars from a galactic globular cluster, we test stars with a metallicity of $[\text{M}/\text{H}] = -0.78$ (Marín-Franch et al. 2009) and lower average mass than what is expected for the solar neighbourhood. Therefore, we study objects with a smaller radius in this case. Although the results from the cluster stars may not be directly applicable to the solar neighbourhood miras, this test helps to derive a better understanding of the EIF for AGB stars.

We adopted the collection of 47 Tuc LPVs by Lebzelter & Wood (2005) to quantitatively test the reliability of their *Gaia* parallax uncertainties. A qualitative test has already been performed by Lebzelter et al. (2023, their Fig. 33), indicating that the parallax uncertainties are at least realistic. From the 42 stars listed in Table 1 of Lebzelter & Wood (2005), we discarded the star LW14, because no parallax is listed in the DR3, and LW12, because its DR3 parallax is about a factor of two larger than the average of all other stars, more than 5σ away from the cluster average, and thus could be a foreground star. On the other hand, we retained V19 that was speculated by Lebzelter & Wood (2005) to

be a foreground star; its parallax is fully compatible with it being a cluster member. We also added V17, which is discussed in the main text of Lebzelter & Wood (2005) but is missing from their Table 1. Thus, we have a sample of 41 LPVs in 47 Tuc available for our parallax uncertainty test. Their *Gaia* parallaxes are about a factor of 10 larger than the associated uncertainties.

As the size of convective cells on the surface increases with decreasing surface gravity, $\log g$ (Paladini et al. 2018), and as parallax uncertainty for AGB stars is likely affected by large convective cells (Chiavassa et al. 2018), we expect that the parallax uncertainty of 47 Tuc LPVs increases with decreasing surface gravity. The surface gravity decreases as a star becomes more luminous. Thus, we expect the parallax uncertainty to increase with K magnitude. The mass loss along the AGB will enhance the effect, but should play a minor role. In the upper panel of Fig. 9, *Gaia* parallax uncertainties of 47 Tuc LPVs are plotted as a function of their mean K band magnitude, adopted from Lebzelter & Wood (2005). We can see that the brightest stars indeed have significantly increased parallax uncertainties. In addition, the fainter stars appear to have parallax uncertainties that increase slowly with K -band brightness.

However, there are some stars that deviate from the trend. The parallax uncertainty may also be enhanced by a high stellar density: El-Badry et al. (2021) found that the parallax uncertainty is enhanced for binaries with projected separations of $\lesssim 4''$. Therefore, we may expect that the parallax uncertainty is enhanced for stars close to the cluster centre where the stellar density is highest. We therefore plot the parallax uncertainty as a function of the angular distance from the cluster centre (r) in the lower panel of Fig. 9. Indeed, we see that the parallax uncertainty is increased at $r \lesssim 2'$. To demonstrate that the parallax uncertainty depends on both the K band magnitude and the distance from the cluster centre, we plot the stars at $r \leq 1'$ as filled symbols in the upper panel and stars $K \leq 6.5$ as filled symbols in the lower panel of Fig. 9.

Independent of the cause for the enhanced parallax uncertainties, we can perform a theoretical test if they are correctly estimated in *Gaia* DR3. For this end, we adopted the same methodology as El-Badry et al. (2021) to estimate the reliability of the parallax uncertainties from binary components and treat each pair of LPVs as components of a binary system. We can neglect the spatial extension of 47 Tuc for our purposes because the half-light radius is only $\sim 2.9'$ (Trager et al. 1993), corresponding to about 3.7 pc, whereas the distance to the cluster is ~ 4.45 kpc. Having $n = 41$ stars thus gives us $n \cdot (n - 1)/2 = 820$ stellar pairs i, j ($i \neq j$) for which we can calculate the quantity

$\Delta\varpi/\sigma_{\varpi,\text{tot}} = (\varpi_i - \varpi_j)/\sqrt{\sigma_{\varpi,i}^2 + \sigma_{\varpi,j}^2}$. For perfectly estimated parallax uncertainties, $\Delta\varpi/\sigma_{\varpi,\text{tot}}$ should follow a normal distribution with a width of 1.0. In reality, we find that the values of $\Delta\varpi/\sigma_{\varpi,\text{tot}}$ distribute with a width of 1.34. The ratio of the standard deviation of the parallaxes to the average parallax uncertainty gives the almost identical value of $0.0300/0.0222 = 1.35$. We may compare this with the parallax uncertainty inflation factors inferred from widely separated pairs by El-Badry et al. (2021, their Eq. 16). Our 47 Tuc LPVs have *Gaia* G band magnitudes in the relatively narrow range between 10.71 and 11.59 . El-Badry et al. (2021) estimate parallax uncertainty inflation factors between 1.11 and 1.16 for this magnitude range. Thus, the parallax uncertainties of the 47 Tuc LPVs are underestimated by a somewhat larger factor than would be expected from this empirical formula, even if all but one of the sample stars have $\text{ruwe} < 1.4$.

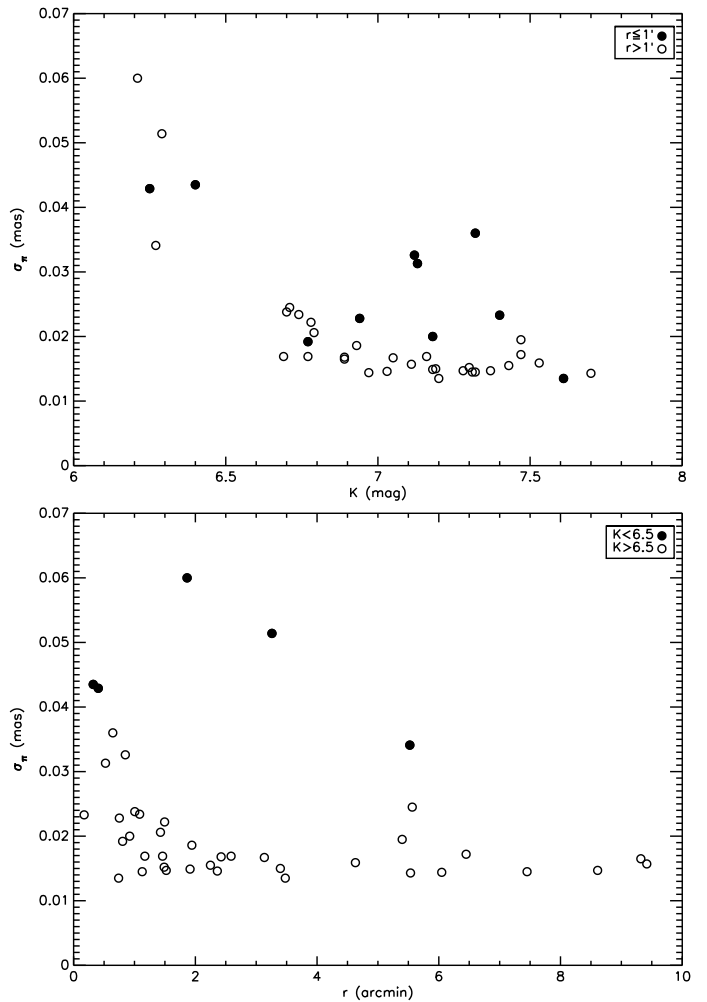


Fig. 9. *Gaia* parallax uncertainties of 47 Tuc LPVs. *Upper panel*: Uncertainty as a function of K band magnitude, which is proportional to the surface gravity $\log g$. Filled symbols show stars closer than $1'$ to the cluster centre, open symbols represent more distant stars. Brighter (i.e., more extended) stars have larger parallax uncertainty because of stronger surface brightness variation. *Lower panel*: Uncertainty as a function of angular distance from the cluster centre r . Filled symbols represent stars brighter than $K = 6.5$, open symbols those fainter than this limit. The half-light radius of 47 Tuc is $\sim 2.9'$. The uncertainty is enhanced close to the cluster centre because of the higher stellar density.

5. Stars with changing pulsation periods

Several Miras and SRVs are known to have pulsation periods that change significantly on timescales of decades or centuries. Templer et al. (2005) find that $\sim 4\%$ of their sample stars change periods at a level $> 3\sigma$, and Merchan-Benitez et al. (2023) studied in more detail their amplitudes of period change. Continuous, sudden, and meandering period changes have been reported in the literature (Zijlstra & Bedding 2002; Uttenthaler et al. 2011). Different mechanisms have been discussed in the literature to explain these period changes. The leading explanation is that continuous and sudden period changes are caused by a recent TP and we see the stars in different phases of the TP (Wood & Zarro 1981). In this picture, a star experiencing a sudden decrease in period undergoes the onset of a TP, while a continuous change corresponds to a later phase of the TP cycle. A third dredge-up event in the aftermath of a TP may also cause a period change, if it happens to increase the atmospheric C/O ratio from $\lesssim 1$ to

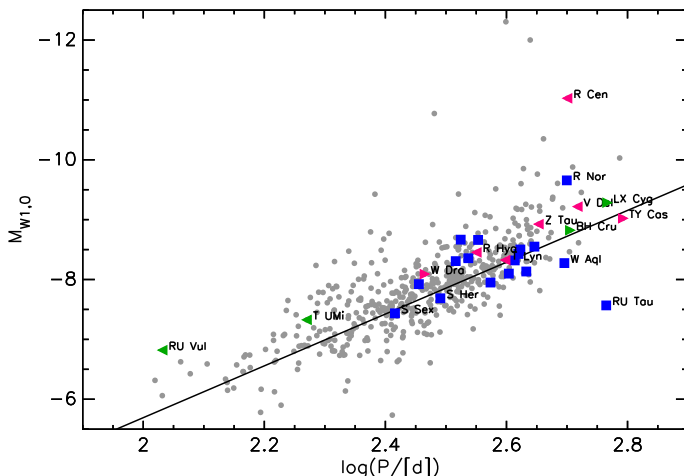


Fig. 10. PL(W1) of all Karlsson Miras, with stars with changing pulsation periods highlighted. Magenta triangles represent Miras with continuously changing periods with the orientation of the triangle indicating increasing (right-pointing) or decreasing (left-pointing) periods, green triangles represent stars with sudden period changes with the same meaning of the triangle orientation, and blue squares represent Miras with meandering periods. RU Vul is the only nominal SRV and is not contained in the Karlsson sample. The grey dots represent all other Miras with relatively stable periods.

> 1 (Uttenthaler et al. 2016b). Merchan-Benitez et al. (2023) found evidence that also the meandering period change could be connected to the effects of TPs.

So far, it is not known where Miras or SRVs undergoing such period changes are located in PL diagrams and whether they follow the PL-relations of stars with stable periods. The data presented in this paper allow us to address this question for the first time. Here, it is of particular importance to have contemporary (IR) photometric observations and period determinations. Figure 10 shows the PL(W1) diagram of all 510 Karlsson Miras with *Gaia* parallax distances. Stars with changing pulsation periods identified in the literature (see the above-cited papers) are highlighted by coloured symbols. The three change types are identified by different symbols and colours. All symbols of stars with continuously and suddenly changing periods are labelled with their names, but only few with meandering periods. Meandering-period stars not labelled in Fig. 10 are RS Aql, AF Car, U CMi, T CMi, TY Cyg, T Hya, S Ori, SS Peg, RU Sco, Z Sco, T Ser, and Z Vel.

A few stars in Fig. 10 do not follow well the relation formed by the other stars. One of them is R Cen, a Mira whose period has continuously decreased from 570 d in 1870 to 505 – 510 d in 2000 (Hawkins et al. 2001). The list of T. Karlsson reports a current period of just over 500 d. The star is thought to be an intermediate-mass star ($M \gtrsim 4M_{\odot}$) undergoing hot bottom burning (HBB; García-Hernández et al. 2013). Such stars are expected to be shifted from the relation formed by lower-mass stars because of their higher mass and the additional luminosity generated by the HBB process (Lebzelter et al. 2019). However, R Cen is shifted from the relation by a large margin. R Nor is a candidate for being an intermediate-mass AGB star undergoing HBB, too, but it is located above the relation by a much smaller amount. The *Gaia* parallax of R Cen is also relatively uncertain, $\sigma_{\varpi}/\varpi \approx 0.22$. We therefore suspect that its *Gaia* distance is overestimated by a considerable amount.

RU Tau has a meandering pulsation period and is also separated from the other Miras. However, it is located much be-

low the relation formed by the other Miras, a locus that it does not share with any other star. Its *Gaia* parallax is also relatively uncertain $\sigma_{\varpi}/\varpi \approx 0.17$, and RU Tau is at a large distance of $d \approx 2.5$ kpc from the sun.

The only non-Mira included in Fig. 10 is RU Vul. It was originally classified as an SRV of subtype a, undergoing a sudden period decrease that commenced in 1954. We include it in Fig. 10 with a period of 108 d measured by Uttenthaler et al. (2016a) from observations obtained between 2011 and 2013. RU Vul is shifted from the fundamental mode PL(W1) relation to shorter period and/or higher luminosity. McDonald et al. (2020) showed that the star is rapidly becoming brighter in the mid-infrared as a result of rapid dust formation close to the star. However, this probably does not affect the W1 band, and the overall luminosity has probably decreased over the last decades (McDonald et al. 2020). The shift to a shorter period could, therefore, be an indication that RU Vul is evolving from the fundamental pulsation mode towards one of the overtone pulsation modes. Similarly, T UMi has been shown by Molnár et al. (2019) to have transitioned to a double-mode pulsation state with a fundamental mode period of just under 200 d at the end of 2018 and a first overtone mode period of 110 d. We include it in Fig. 10 with a period of ~ 190 d as listed by T. Karlsson, corresponding to the fundamental mode period. Thus, RU Vul and T UMi could be experiencing the same evolutionary phenomenon.

Besides these few outliers, all other stars appear to follow the PL(W1) relation relatively closely. Many of the stars with changing pulsation periods are actually contained in the gold sample defined above. Therefore, we can conclude with some confidence that Mira stars with changing pulsation periods, in general, follow the fundamental mode PL(W1) relation relatively closely. In turn, this means that the distances of Miras with changing pulsation periods can be inferred from their pulsation periods and apparent (IR) magnitudes with reasonable accuracy, provided that these quantities are observed at the same time and the star has not yet moved to overtone pulsation.

6. Discussion and conclusions

We collected high-quality, hand-picked data of solar-neighbourhood Miras to construct their PL-relations in nine near-IR bands, most of them for the first time. Our database was allocated from two multi-epoch IR catalogues, namely the COBE/DIRBE catalogue of variable stars of Price et al. (2010) and the WISE/unTimely catalogue of Meisner et al. (2023). The pulsation periods of the stars were adopted from Karlsson (2013), who determined them from contemporaneous optical observations. These data were combined with *Gaia* DR3 parallax distances derived and published by Bailer-Jones et al. (2021). The stars in the gold sample, defined to have relative parallax uncertainties $\leq 10\%$, form well-defined PL-relations without sigma-clipping or further removal of outliers, except for one temporarily obscured C star (Sect. 3.1). Comparison with data from the literature of the PL-relations of (O-rich) Miras in the more metal-poor LMC confirms that the Galactic Miras are fainter than the LMC Miras by up to $0^m2 - 0^m3$ in those bands, and that the PL-relations of Galactic Miras are steeper than those of LMC Miras (Sect. 3.2).

In Sect. 3.3, we constructed synthetic SEDs based on the nine PL-relations established before. We fitted the SEDs at six $\log(P)$ values representative for our sample stars with a black-body curve. The WISE bands were excluded from the fit because they significantly deviated from the Planck curve, indicating remaining issues with reconstructing the flux of these bright,

partly saturated sources. From the blackbody fit, we derived the period–temperature, period–bolometric-luminosity, and period–radius relations; see Eqs. 4–6. They may be useful as empirical relationships for other studies of AGB variables.

We also used our data to investigate whether the parallax uncertainties of Mira stars given in *Gaia* DR3 are underestimated. Mira variables are very extended stars with low surface gravity and are thought to have large convective cells on their photospheres, resulting in significant surface brightness variations. These variations may impact the position measurements used for the parallax determination. The literature suggests that the parallax uncertainties of AGB stars in general and Mira variables in particular are significantly underestimated (Van Langevelde et al. 2018; Andriantsaralaza et al. 2022). We used three different approaches in this work to test the *Gaia* parallax uncertainties. The first one (Sect. 4.1) uses the observed scatter of stars around the $PL(K)$ relation: If the true parallax uncertainties were considerably larger than the one quoted in the *Gaia* catalogue, we may expect to observe an ill-defined PL-relation of Miras. We applied a small grid of COLIBRI evolutionary tracks to model the intrinsic width of the fundamental mode PL-relation for a solar neighbourhood sample due to stellar evolution on the AGB and the range of initial masses. The result of this test is that the error inflation factor (EIF) to be applied to the parallax uncertainties is consistent with 1.0, meaning that the original *Gaia* uncertainties are realistic. An even better agreement between observed and modelled scatter is reached for an EIF of 1.3, and an EIF of 1.7 marginally agrees with the observations. This test is not highly stringent, and we discuss the shortcomings of the evolutionary grid used to model the scatter. Nevertheless, it indicates that large EIFs (> 2), as reported in the literature, are very unlikely.

The second test (Sect. 4.2) compares the *Gaia* parallaxes and their uncertainties to the respective measurements derived from VLBI observations. Before applying this test, we improved on the pulsation periods of the stars in the common sample. With the improved periods, the Miras form a very well-defined PL-relation in the WISE $W1$ band that extends to the longest periods ($P \gtrsim 1000$ d). This indicates that long-period OH/IR stars follow the same near-IR PL-relation as shorter-period Miras as long as circumstellar dust does not significantly diminish the light in the chosen photometric band. Restricting the common sample to stars that have relative parallax uncertainties $\leq 10\%$ in both catalogues and removing two further significant outliers reduces the EIF of the *Gaia* parallax uncertainties to ~ 2.3 (Table 5). However, for a faint sample, the EIF is reduced to ~ 1.8 . These factors apply only if one assumes that the VLBI parallax uncertainties are reliable and do not require an inflation factor. VERA Collaboration et al. (2020) concede that the VLBI parallax error analysis differs from paper to paper, and that the formal uncertainty could underestimate the error in the averaged parallax value if systematic errors from atmospheric phase fluctuation are not fully taken into account. Thus, rather than the one-sided EIF, the two-sided EIF estimated in this work might be more applicable. We also caution that this test relies on a relatively small sample of stars with VLBI parallaxes because they are laborious to measure.

The third and final test is applied to a sample of 41 LPVs on the AGB of the globular cluster 47 Tuc. This sample of stars can be considered to be located at an identical distance from the sun, and if their parallax uncertainties are estimated correctly, their spread in measured distances and combined parallax uncertainties should agree on a statistical level. This test is the most stringent of the three and results in an EIF of 1.34. The disadvantage

of this test, however, is that the sample stars are relatively low-mass and metal-poor; thus, they are not as extended as the more massive and metal-rich solar-neighbourhood Miras.

All three tests suggest EIFs of the *Gaia* parallax uncertainties of AGB stars in the range of 1.0 to 1.8. An EIF of 1.3 appears to be a reasonable consensus. This may be compared to the peak EIF of 1.3 found by El-Badry et al. (2021) from the analysis of resolved binaries in the *Gaia* catalogue. However, at $G = 13^m$, this peak is at a fainter G band magnitude than most of our Miras are on average. We rule out significantly larger EIFs with high confidence, but more tests on the reliability of the *Gaia* parallax uncertainties of AGB stars are highly welcome.

As one can appreciate from Figs. 8 and 10, stars with relatively uncertain parallaxes ($\sigma_{\varpi}/\varpi > 0.1$) tend to be located above the PL-relation formed by the gold sample stars with precise parallaxes. We confirmed this by inspecting the location of stars with $\sigma_{\varpi}/\varpi > 0.1$ in the $PL([2.2])$ and $PL(W1)$ diagrams: On average, the stars are above the best-fit line by $\sim 0^m6$ and $\sim 0^m3$, respectively. This means that the distances of AGB stars with larger uncertainties tend to be overestimated in the catalogue of Bailer-Jones et al. (2021). However, as the range of deviation from the PL-relations is large, it is difficult to derive a general law to improve parallax distance estimates of Miras.

Finally, we inspected the location of Miras with changing pulsation periods in the $PL(W1)$ diagram. We showed that Miras with changing pulsation periods follow the fundamental mode $PL(W1)$ relation formed by other stars relatively closely, except for a few outliers. Thus, their distances can be inferred from their pulsation periods and apparent IR magnitudes with reasonable accuracy if periods and mean magnitudes are measured contemporaneously.

Acknowledgements. We thank Aaron Meisner for help with the WISE/unTimely photometry. This research was funded in part by the Austrian Science Fund (FWF) 10.55776/F8100. For open access purposes, the author has applied a CC BY public copyright license to any author accepted manuscript version arising from this submission. We acknowledge with thanks the variable star observations from the AAVSO International Database contributed by observers worldwide and used in this research. This work has made use of data from the European Space Agency (ESA) mission *Gaia* (<https://www.cosmos.esa.int/gaia>), processed by the *Gaia* Data Processing and Analysis Consortium (DPAC, <https://www.cosmos.esa.int/web/gaia/dpac/consortium>). Funding for the DPAC has been provided by national institutions, in particular the institutions participating in the *Gaia* Multilateral Agreement. This publication makes use of data products from the Two Micron All Sky Survey, which is a joint project of the University of Massachusetts and the Infrared Processing and Analysis Center/California Institute of Technology, funded by the National Aeronautics and Space Administration and the National Science Foundation. This publication makes use of data products from the Wide-field Infrared Survey Explorer, which is a joint project of the University of California, Los Angeles, and the Jet Propulsion Laboratory/California Institute of Technology, funded by the National Aeronautics and Space Administration.

References

- Andriantsaralaza, M., Ramstedt, S., Vlemmings, W. H. T., & De Beck, E. 2022, *A&A*, 667, A74
- Bailer-Jones, C. A. L., Rybizki, J., Fouesneau, M., Demleitner, M., & Andrae, R. 2021, *AJ*, 161, 147
- Chiavassa, A., Freytag, B., & Schulteis, M. 2018, *A&A*, 617, L1
- El-Badry, K., Rix, H.-W., & Heintz, T. M. 2021, *MNRAS*, 506, 2269
- Engels, D., Etoka, S., Jiménez-Esteban, F., Herrmann, W., & López-Martí, B. 2024, in IAU Symposium, Vol. 376, IAU Symposium, ed. R. de Grijs, P. A. Whitelock, & M. Catelan, 328–333
- Feast, M. W., Whitelock, P. A., Catchpole, R. M., Roberts, G., & Overbeek, M. D. 1984, *MNRAS*, 211, 331
- Finkbeiner, D. P., Padmanabhan, N., Schlegel, D. J., et al. 2004, *AJ*, 128, 2577
- Gaia Collaboration, Vallenari, A., Brown, A. G. A., et al. 2023, *A&A*, 674, A1
- García-Hernández, D. A., Zamora, O., Yagüe, A., et al. 2013, *A&A*, 555, L3
- Glass, I. S. & van Leeuwen, F. 2007, *MNRAS*, 378, 1543

Gontcharov, G. A. 2017, *Astronomy Letters*, 43, 472

Groenewegen, M. A. T. 2021, *A&A*, 654, A20

Groenewegen, M. A. T. 2022, *A&A*, 659, A145

Hawkins, G., Mattei, J. A., & Foster, G. 2001, *PASP*, 113, 501

Heinze, A. N., Tonry, J. L., Denneau, L., et al. 2018, *AJ*, 156, 241

Huang, C. D., Yuan, W., Riess, A. G., et al. 2024, *ApJ*, 963, 83

Iwanek, P., Kozłowski, S., Gromadzki, M., et al. 2021a, *ApJS*, 257, 23

Iwanek, P., Soszyński, I., & Kozłowski, S. 2021b, *ApJ*, 919, 99

Karlsson, T. 2013, *JAAVSO*, 41, 348

Kroupa, P. 2001, *MNRAS*, 322, 231

Lebzelter, T., Mowlavi, N., Lecoeur-Taibi, I., et al. 2023, *A&A*, 674, A15

Lebzelter, T., Mowlavi, N., Marigo, P., et al. 2018, *A&A*, 616, L13

Lebzelter, T., Trabucchi, M., Mowlavi, N., et al. 2019, *A&A*, 631, A24

Lebzelter, T. & Wood, P. R. 2005, *A&A*, 441, 1117

Lenz, P. & Breger, M. 2004, in *IAU Symposium*, Vol. 224, *The A-Star Puzzle*, ed. J. Zverko, J. Ziznovsky, S. J. Adelman, & W. W. Weiss, 786–790

Lindgren, L., Klioner, S. A., Hernández, J., et al. 2021, *A&A*, 649, A2

Maehara, H. 2014, *JAXA-RR*, 3, 119

Marigo, P., Bossini, D., Trabucchi, M., et al. 2022, *ApJS*, 258, 43

Marigo, P., Bressan, A., Nanni, A., Girardi, L., & Pumo, M. L. 2013, *MNRAS*, 434, 488

Marín-Franch, A., Aparicio, A., Piotto, G., et al. 2009, *ApJ*, 694, 1498

McDonald, I., Uttenthaler, S., Zijlstra, A. A., Richards, A. M. S., & Lagadec, E. 2020, *MNRAS*, 491, 1174

Meisner, A. M., Caselden, D., Schlafly, E. F., & Kiwy, F. 2023, *AJ*, 165, 36

Merchan-Benítez, P., Uttenthaler, S., & Jurado-Vargas, M. 2023, *A&A*, 672, A165

Molnár, L., Joyce, M., & Kiss, L. L. 2019, *ApJ*, 879, 62

Mowlavi, N., Trabucchi, M., & Lebzelter, T. 2019, in *The Gaia Universe*, 62

Nakagawa, A., Kurayama, T., Matsui, M., et al. 2016, *PASJ*, 68, 78

Nakagawa, A., Kurayama, T., Orosz, G., et al. 2018, in *IAU Symposium*, Vol. 336, *Astrophysical Masers: Unlocking the Mysteries of the Universe*, ed. A. Tarchi, M. J. Reid, & P. Castangia, 365–368

Nakagawa, A., Morita, A., Sakai, N., et al. 2023, *PASJ*, 75, 529

Paladini, C., Baron, F., Jorissen, A., et al. 2018, *Nature*, 553, 310

Pietrzynski, G., Graczyk, D., Galleine, A., et al. 2019, *Nature*, 567, 200

Pojmanski, G. 2002, *Acta Astron.*, 52, 397

Price, S. D., Smith, B. J., Kuchar, T. A., Mizuno, D. R., & Kraemer, K. E. 2010, *ApJS*, 190, 203

Riebel, D., Meixner, M., Fraser, O., et al. 2010, *ApJ*, 723, 1195

Sanders, J. L. 2023, *MNRAS*, 523, 2369

Schlafly, E. F., Meisner, A. M., & Green, G. M. 2019, *ApJS*, 240, 30

Skiff, B. A. 2014, *VizieR Online Data Catalog*, B/mk

Skrutskie, M. F., Cutri, R. M., Stiening, R., et al. 2006, *AJ*, 131, 1163

Smith, B. J., Price, S. D., & Baker, R. I. 2004, *ApJS*, 154, 673

Soszyński, I., Udalski, A., Kubiak, M., et al. 2004, *Acta Astronomica*, 54, 129

Soszyński, I., & Wood, P. R. 2013, *ApJ*, 763, 103

Templeton, M. R., Mattei, J. A., & Willson, L. A. 2005, *AJ*, 130, 776

Trabucchi, M., Wood, P. R., Montalbán, J., et al. 2017, *ApJ*, 847, 139

Trabucchi, M., Wood, P. R., Mowlavi, N., et al. 2021, *MNRAS*, 500, 1575

Trager, S. C., Djorgovski, S., & King, I. R. 1993, in *Astronomical Society of the Pacific Conference Series*, Vol. 50, *Structure and Dynamics of Globular Clusters*, ed. S. G. Djorgovski & G. Meylan, 347

Udalski, A. 2003, *Acta Astronomica*, 53, 291

Uttenthaler, S., Greimel, R., & Templeton, M. 2016a, *Astronomische Nachrichten*, 337, 293

Uttenthaler, S., Meingast, S., Lebzelter, T., et al. 2016b, *A&A*, 585, A145

Uttenthaler, S., van Stiphout, K., Voet, K., et al. 2011, *A&A*, 531, A88

Van Langevelde, H., Quiroga-Nuñez, L. H., Vlemmings, W. H. T., et al. 2018, in *14th European VLBI Network Symposium & Users Meeting (EVN 2018)*, 43

VERA Collaboration, Hirota, T., Nagayama, T., et al. 2020, *PASJ*, 72, 50

Vlemmings, W. H. T., van Langevelde, H. J., Diamond, P. J., Habing, H. J., & Schilizzi, R. T. 2003, *A&A*, 407, 213

Watson, C. L., Henden, A. A., & Price, A. 2006, *Society for Astronomical Sciences Annual Symposium*, 25, 47

Whitelock, P., Feast, M., & Catchpole, R. 1991, *MNRAS*, 248, 276

Whitelock, P. A., Feast, M. W., & Van Leeuwen, F. 2008, *MNRAS*, 386, 313

Wood, P. R. 2000, *PASA*, 17, 18

Wood, P. R. & Zarro, D. M. 1981, *ApJ*, 247, 247

Wright, E. L., Eisenhardt, P. R. M., Mainzer, A. K., et al. 2010, *AJ*, 140, 1868

Xue, M., Jiang, B. W., Gao, J., et al. 2016, *ApJS*, 224, 23

Yuan, W., He, S., Macri, L. M., Long, J., & Huang, J. Z. 2017, *AJ*, 153, 170

Zijlstra, A. A. & Bedding, T. R. 2002, *JAAVSO*, 31, 2